Materials Science in Semiconductor Processing 176 (2024) 108320

Contents lists available at ScienceDirect

Materials Science in Semiconductor Processing

journal homepage: www.elsevier.com/locate/mssp

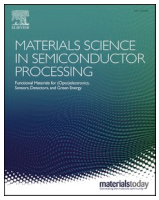

On the prospects of using B_4C_3 as a potential electrode material for lithium-ion batteries

Abdul Majid [a,*], Usama Najam [a], Sheraz Ahmad [a], Mohammad Alkhedher [b]

[a] Department of Physics, University of Gujrat, Gujrat, 50700, Pakistan
[b] Mechanical and Industrial Engineering Department, Abu Dhabi University, Abu Dhabi, 59911, United Arab Emirates

ARTICLE INFO

Keywords:
Lithium ion battery
Anode
Electrochemical properties
Density functional theory
B_4C_3

ABSTRACT

Lithium-ion batteries (LIBs) served as promising energy-storage solutions for various applications, from portable electronics to electric-vehicles. There is a growing demand for high-performance electrode materials with improved storage capacity, high cyclic stability, low energy barriers, reduced material toxicity, and cost-effectiveness. This study explores the electrochemical feasibility of B_4C_3 monolayer as an anode material for LIBs using density functional theory (DFT) computations and molecular dynamic (MD) simulations. The optimum anodic nature of B_4C_3 is reported based on its structural, electronic, diffusion, storage behaviour, and lithiation studies. The adsorption sites for Li atoms were systematically explored. The lithium saturation requires the adsorption of 29 lithium atoms on B_4C_3 while preserving stability confirmed by Ab-initio molecular dynamics (AIMD) simulations and ensuring favorable transport characteristics during the lithiation process based on Hirshfeld charge analysis and steric interaction calculations. The storage capacity of the host B_4C_3 is calculated as 2770.2 $mAhg^{-1}$ which is notably higher than that of graphite anode. The computed value of open circuit voltage is 0.62 V per Li. The value of diffusion coefficient and ionic conductivity σ is 0.7 × 10^{-8} m^2/s and 0.78 S/m respectively which predicts excellent overall anodic operation of the material. The transition barrier of the Li ions in the material is determined through Cl-NEB, which shows the lowest value of 0.06 eV along the x-axis.

1. Introduction

The demand for affordable and environmentally sustainable energy sources is a fundamental necessity in the current era of innovations and technology [1]. The considerable dimensions and weight of energy storage media pose a challenge to their transportation. The widespread use of electronic devices in contemporary times has increased the emphasis on developing lightweight and portable batteries [2]. The vehicle industry heavily relies on petrol as a primary energy source, which has caused environmental contamination and contributed to global warming. Therefore, researchers contemplate exploring novel and dependable energy sources [3]. Portable and rechargeable batteries are widely used, particularly in electronic gadgets [4]. Lithium-ion batteries (LIBs) technology has emerged as a potential option for mobile power sources owing to its cost-effectiveness, exceptional cycle life, power density, reversible capacity and high efficiency [5,6]. However, the existing commercial LIBs are inadequate to meet the rapidly increasing demands of energy-storage.

Several challenges must be addressed, including low Columbic-efficiency, structural defects instigated by impurities and degradation over time [7]. The electrode materials in LIBs are essential factors that affect overall electrochemical performance, especially the anode material that stores charges. Graphite has been utilized as an anode in LIBs, but its storage capacity is just 372 $mAhg^{-1}$ [8]. The presence of impurities results in a reduced charge density as the Li ions are trapped by these impurities, leading to a decline in battery efficiency [9]. The graphite exhibits specific stability concerns in such a way that structural collapse in lower dimensional systems may occur after undergoing multiple cycles of charging and discharging [10]. These drawbacks disqualify its applications in future electrical vehicles and electricity grids.

Anodes based on lithium alloy have been employed in LIBs yet are plagued by volumetric expansion [11]. Several two-dimensional (2D) materials exhibited promise as anode for LIBs owing to their remarkable properties [12]. Firstly, their satisfactory atomic thickness results in minimal volume expansion, contributing to excellent cycle ability. Secondly, only a few dangling-bonds on the surface lowers the diffusion barrier, leading to high charge-discharge rates [13]. Thirdly, weak

* Corresponding author.
E-mail address: Abdulmajid40@yahoo.com (A. Majid).

https://doi.org/10.1016/j.mssp.2024.108320
Received 21 November 2023; Received in revised form 21 February 2024; Accepted 8 March 2024
Available online 13 March 2024

surface interactions result in a low binding-energy [14]. Lastly, the ample adsorption sites facilitated by the high surface-to-mass ratio of 2D materials contribute to a substantial energy storage capacity [15]. First-principles calculations have been utilized to elucidate the characteristics of various 2D materials when employed as anode for LIBs. The researchers are still working to boost LIBs performance by presenting novel composites, such as carbon nanotubes and carbon-silicon compounds [16].

There are numerous 2D materials, such as MoS_2, graphene [17–19], phosphorene [20], transition-metal dichalcogenides [21] and Mxenes [22], that exhibit flat surfaces, high surface areas, and abundant adsorption sites. These materials have shown great promise as an anode for LIBs, offering high-energy densities and excellent rate capability. Significant research endeavours have been dedicated to discovering novel carbon-based materials capable of attaining high capacity [23]. The processes of material engineering, alloying, doping, and nano-structuring of the materials appeared to enhance the storage capacity of the materials based on an increase in surface area, reduction in diffusion barrier, and upgrading of the transport properties [24].

Borophene, among the renowned 2D materials with its impressive electric conductivity, lightweight nature, and remarkable properties, is increasingly recognized as a viable option for alternative electrode materials in energy storage devices [25]. By conducting comprehensive density functional theory (DFT) calculations, the adsorption and diffusion characteristics of borophene have been investigated, which showcased its potential as a viable anode material for LIBs or sodium-ion batteries (NIBs) [26]. Demonstrating impressive electrochemical performance, the capacity device based on a few-layer borophene extends across a broad potential up to 3 V. It is particularly interesting for showcasing a remarkable energy density of 46.1 Wh/kg alongside a power density of 478.5 Wh/kg. The device demonstrates impressive resilience, retaining 88.7% of its initial particular capacitance throughout 6000 cycles [27]. The 2D allotropes of boron-doped carbon BC_x in sheets have been reported to exhibit a maximum number of hexagons [28].

The effectiveness of B-doped graphene surpassed that of pure graphene. The studies indicate that incorporating boron in graphite can be used as an anode as an alternative to traditional graphite [29]. B_4C revealed improved reversibility due to its enhanced conductivity and lowered diffusion barrier despite having a low capacity of 315 $mAhg^{-1}$ [30]. The monolayer of BC_3 demonstrated Li storage capacity approximately 2.5 times higher than graphite [31]. The contemporary era has witnessed a surge in the utilization of various 2D materials owing to their prospective applications [32,33]. 2D BeB_2 monolayer has been reported as having a capacity of 1749.8 mAh/g with an open circuit voltage (OVC) of 0.33 V [34]. Boron-based 2D carbonaceous material B_2C monolayer has been reported to have a capacity of 1596 mAh/g with a transition energy barrier of 0.49 V and OCV of 0.57 V [35]. The capacity, open circuit voltage, adsorption energy, and energy barrier of recently used 2D monolayers as anode materials in LIBs are listed in Table 1.

Boron carbide (B_4C_3) is relatively obscure within the series of reported 2D materials [36]. This study comprehensively analyzes the electrochemical behaviour of the B_4C_3 monolayer in LIBs. The structural characteristics of B_4C_3 are remarkable and show exceptional stability [37]. Furthermore, the electronic, diffusion, conductivity, voltage profile and Li intercalation study of B_4C_3 points out the suitability of B_4C_3 monolayer as an anode for LIBs with improved performance [38].

2. Methodology

This study employed Density Functional Theory (DFT) utilizing the BAND and DFTB codes in Amsterdam density functional (ADF) package to assess the structural, electronic, and conduction characteristics of B_4C_3 monolayer as a potential candidate in Lithium-ion batteries (LIBs). The graphical user interface (GUI) configures data file structures and adjusting settings. The calculations utilize the Grimme D3 correction with generalized gradient approximation (GGA) and Perdew–Burke–Ernzerhof (PBE), incorporating the electron-nucleus interactions and electronic exchange correlations. The structural optimization is performed using the quasi-Newton method, with a step size of 0.001 and a convergence requirement of 10^{-5} eV/atom. ADF's Triple Zeta Polarized (TZP) functions were employed for the basis sets formation. The numerical quality was set as good, based on Becke fuzzy cell integration under frozen core approximation. The SCF relies on the Direct Inversion of Iterative Subspace method (DIIS), which incorporates a highly optimized numerical integration scheme for Hamiltonian evaluation [31]. The convergence of atomic positions is achieved by considering energy and force criteria below 0.00027 eV and 0.027 eV/Å, respectively. The energy values were exclusively assessed through single-point (SP) runs, which involved calculating the derivatives of the Hessian and nuclear gradients.

The lithiation energy plays a crucial role in accessing the behavior of the B_4C_3 monolayer as an anode in LIBs. It determines the nature of the reaction, whether it is exothermic or endothermic and involves positioning Li atoms above and below the B_4C_3 monolayer. The calculation of lithiation energy follows the formula presented in Equation (1).

$$E_{Formation} = E_{LixB4C3} - x * E_{Li} - E_{B4C3} \quad (1)$$

Where $E_{Formation}$ denotes the formation energy obtained upon intercalation of Li atoms in the host to check the feasibility of the reaction (exothermic or endothermic), $E_{LixB4C3}$ represents the energy of Li-intercalated B_4C_3 system. E_{Li} points to the energy of an individual lithium atom obtained from geometry optimization of bulk lithium metal in BCC structure, x denotes the number of lithium atoms involved in the simulation, and E_{B4C3} corresponds to the energy of the optimized

Table 1
The comparison of electrochemical parameters of contemporary materials used in LIBs.

Material	Capacity (mAh/g)	E_{ad} (eV)	V_{oc}	No of Li adsorbed	Energy barrier (eV)	Reference
B_4C_3	2770.21	−0.89	0.62 V	29	0.06	Current study
MgB_2 monolayers	1750.9	–	0.697	–	–	[34]
Arsenene monolayer	1430	−2.55	–	–	0.16	[47]
VS_2 monolayer	466	–	0.93	–	–	[48]
FeSe monolayer	658	–	0.38–0.88	–	–	[49]
TiC_3 monolayer	1916	–	0.26	–	0.25	[50]
Zr_2 B_2 monolayer	526	−0.628 eV	–	–	–	[51]
Mn_2C monolayer	887.6	–	0.45–0.15	–	–	[52]
B_7P_2 monolayer	3117	–	–	–	–	[53]
Biphenylene monolayer	1302	−0.44 to −0.15	–	–	0.23	[54]
YS_2 monolayer	350	−2.038	–	–	0.33	[55]
TiOF monolayer	970	–	–	–	0.15/0.14	[56]
FeB_6 monolayer	991	2.89	–	–	0.24	[57]
Ca_2C-ML sheet monolayer	582	–	0.10	–	0.027	[58]
Ti_2BN monolayer	889	–	0.24	–	0.024	[59]

host structure. Furthermore, the AIMD calculations were carried out to validate the findings on the process of lithiation using Equation (1).

Theoretical capacity is a crucial indicator of accessing the electrode performance. Equation (2) is used to determine the theoretical capacity of the material.

$$C = \frac{x * F}{M_{LixB4C3}} \tag{2}$$

Where C is the capacity of the material, while x refers to the number of lithium atoms, F is the Faradays constant and $M_{LixB4C3}$ is the mass of the host substance, including the lithium atom placed over it.

To calculate the OCV, a crucial parameter to evaluate anode feasibility in LIBs, hybrid grand canonical Monte Carlo/molecular dynamics (GCMC/MD) simulations are carried out. The OCV is calculated using Equation (3).

$$V = \frac{E_{Li_{x2}B_4C_3} - E_{Li_{x1}B_4C_3} - (x_2 - x_1)\mu_{Li}}{(x_2 - x_1)e} \tag{3}$$

Where $E_{Li_{x2}B_4C_3}$ and $E_{Li_{x1}B_4C_3}$ are the optimized energies of the lithiated monolayer with x_2 and x_1 concentrations of Li and μ_{Li} denotes Li chemical-potential.

The climbing image nudged elastic band (Cl-NEB) method evaluates energy obstacles to Li-ion diffusion. During lithiation on the B_4C_3 sheet, determining the convex hull as a function of Li concentrations considers all feasible distinct sites for Li assimilation for the given concentration. The NEB approach defines a path that connects the reaction's initial and end states. A succession of intermediate images is then placed along this path, joining a system's initial and final states. Reducing the energy of each image involves adhering to a set of constraints ensuring both path continuity and uniform spacing among the images. The energy barrier for the process is calculated based on the energy span across the images. This method can provide a comprehensive outlook of the reaction and help calculate the energy barrier the host provides [39,40]. We consider eight intermediate images during the simulations and the force on each image supposed image (ith image) is calculated by Equation (4).

$$F_i = \left|F_i^s\right|_{\parallel} - \left|\nabla E(R_i)\right|_{\perp} \tag{4}$$

Where the spring restoring force is represented by $\left|F_i^s\right|_{\parallel}$, the actual force is shown by $\left|\nabla E(R_i)\right|_{\perp}$, and F_i is the total of all forces on the image under consideration. Equation (5) computes the highest energy value of the image under consideration.

$$F_{imax} = \nabla E(R_{imax}) + 2\nabla E|R_{imax}|_{\parallel} \tag{5}$$

Molecular dynamics (MD) simulations were conducted in the NVT ensemble at a temperature range of 300 K–900 K, employing short intervals of 0.25 fs to explore how the materials respond to variations in temperature. The temperature control was achieved by using an NHC (Nose-Hoover Chain) thermostat.

$$MSD = \langle |r(t) - r(0)|^2 \rangle \tag{6}$$

$$D(T) = D_o \exp - \left(\frac{E_a}{kT}\right) \tag{7}$$

In Equation (6), MSD (mean square distance) signifies the average distance travelled by Li, where "r(0)" denotes the initial position, and "r(t)" represents the final location of the particle. The diffusion coefficient D as a function of temperature T is determined by plotting D against 1/T using the Arrhenius relationship. The pre-exponential factor is denoted as D_o , activation energy as E_a, Boltzmann constant as k, and temperature is represented by T in Equation (7).

To examine the interaction of Li with the host monolayer, we determine the ionic conductivity (σ) using the Nernst-Einstein formalism [41,42], as outlined in Equation (8).

$$\sigma = \frac{nq^2}{K_b T} D \tag{8}$$

Where σ represents ionic conductivity, n denotes the number of ions participating in the conductivity mechanism, q means the charge of ions, K_b stands for the Boltzmann constant, T corresponds to the temperature during which the simulations are conducted, and D is diffusion coefficient.

3. Result and discussion

Calculations were conducted to examine the framework, structural, electronic, Li intercalation, diffusion characteristics, and conductivity of a B_4C_3 monolayer as anode in LIBs. The ensuing results and elucidated mechanisms are deliberated in the subsequent sections.

3.1. Structural properties

The calculations were carried out to optimize the B_4C_3 monolayer which comprises of a hexagonal arrangement reminiscent of graphene. The B_4C_3 structure, although not perfectly flat, demonstrates a discernible buckled pattern. The unit cell of B_4C_3 consists of 6 carbon and 8 boron atoms, as shown in Fig. 1. Each carbon atom has four adjacent boron atoms and every boron atom has three adjacent carbon atoms. Boron atoms are coordinated in two patterns, denoted as B1 and B2, respectively. B1 atoms are at the centre in hexa coordination, interacting with three surrounding carbon atoms and three B2 atoms. On the other hand, B2 atoms at the corners of the hexa structure display tetra coordination, forming bonds with one B1 atom and three carbon atoms. The calculated lattice parameters for the B_4C_3 monolayer are a = 9.33 Å and b = 16.2 Å, with an area of 151.2 $Å^2$. This calculation reveals a B1–B2 bond length of 1.67 Å and B–C bonds exhibit three distinct types due to various geometric positions: (a) B2–C bonds (1.50 Å), linking the adjacent B_4C_3 cluster, (b) B2–C bonds (1.53 Å) at the corner of the rings, and (c) B1–C bonds (1.57 Å). The lengths of these B–C bonds lie in the range of 1.50–1.57 Å and the results are consistent with the literature [43]. These findings suggest a robust boron-carbon atom connection in this structure, with all carbon atoms exhibiting tetra coordination in this monolayer that bridges the B_4C_3 cluster. A 2x2 monolayer of B_4C_3 with 56 atoms (24 carbon atoms and 32 boron atoms) is simulated for further calculations, as shown in Fig. 4 (c).

3.2. Electronic properties

To study the Li interaction with the host B_4C_3 monolayer, the electronic properties were calculated before and after the intercalation process. The results reveal B_4C_3 as a semiconductor with a band gap of 2

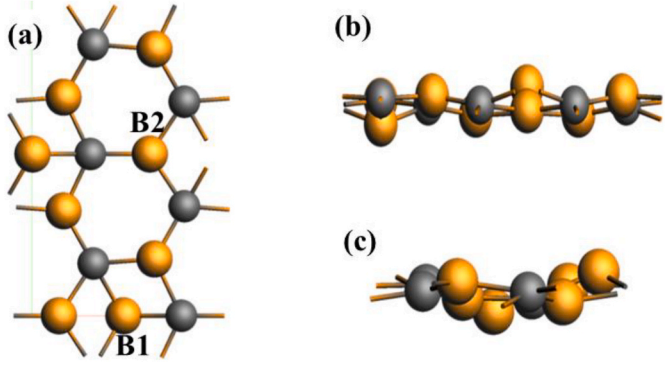

Fig. 1. Optimized unit cell of B_4C_3 monolayer (a) along the z-axis, (b) along the y-axis and (c) along the x-axis. The grey spheres indicate carbon atoms, and the golden spheres represent boron atoms.

eV consistent with the literature [44–46]. Fig. 2 illustrates the density of states (DOS) plots of the B_4C_3 monolayer and 1 Li intercalated B_4C_3 monolayer. Fig. 2 (a) represents the TDOS of B atoms and Fig. 2 (b) represents the TDOS of C atoms in the host monolayer, showing that Carbon atom states contribute more to B_4C_3 than B atoms. In Fig. 2 (c), S-DOS and P-DOS calculations show that p-orbitals are preferentially involved in forming valence and conduction bands than s-orbitals. The valence band exhibits a slight overlap with the Fermi level, suggesting the characteristic n-type semiconducting behavior of the material.

Fig. 2 (d) displays the graph for total DOS (TDOS) and partial DOS (PDOS) with the inclusion of one lithium atom in B_4C_3 to examine how Li atoms affect the DOS in the host material. After the Li adsorption, the peaks get sharper, showing that Li s-states interact with the s and p states of host B_4C_3, transferring their charge to the host structure. This results in a reduction of band gap value and the peaks are shifted toward the conduction band due to the appearance of new Li-2s states after the intercalation process.

The band structure of the host monolayer (pure) and one Li intercalated monolayer is shown in Fig. 3 (a) and 3 (b), respectively. The graphs demonstrate that with the introduction of lithium atoms into the host material, specific states shift toward the Fermi level (from the valence band to the conduction band). This shift is attributed to the intercalation of Li atoms and the involvement of Li-2s states in the host material. It leads to a reduction in the material's band gap.

3.3. Dynamical and thermal stability

A critical aspect of theoretically predicted structures is their dynamical stability. Phonon scattering curves are utilized to examine the dynamic resilience of the B_4C_3 monolayer. In Fig. 4 (a), the phonon band structure of the B_4C_3 monolayer is depicted, revealing the absence of imaginary frequencies across the entire Brillouin zone, signifying the dynamic stability of the structure. To assess the thermal stability of the B_4C_3 monolayer, Ab-initio molecular dynamics (AIMD) calculations were conducted at temperature range up to 900 K. A $2 \times 2 \times 1$ supercell containing 126 atoms was utilized for AIMD calculations for 25 ps, with a temporal interval of 0.25 fs. Fig. 4 (b) illustrates the energy and temperature plotted against time. Notably, the energy of the system remains nearly constant throughout simulations. Snapshots of the structures after 25 ps are presented in Fig. 4 (c). The structure remains intact, exhibiting no bond breakage and affirming the stability of the monolayer.

3.4. Intercalation sites

One lithium is positioned at several high-symmetry locations in the host B_4C_3 monolayer to study the most favorable intercalation site. The site that gives the minimum energy calculated by Equation (1) will be the most promising site for intercalation and will be used for further increased Li concentration. There are six high symmetry sites for Lithium intercalation in the host monolayer represented in Fig. 5 (a) to 5 (f). Fig. 5 (a) illustrates site S1: That ring is vacant in the center of the hexagonal ring made by C and B atoms. Fig. 5 (b) shows site S2: In the 2nd type of ring over the B atom, Fig. 5 (c) shows site S3: Between the B and C atoms over their bond, Fig. 5 (d) represents site S4: Among four B atoms and over a C atom, Fig. 5 (e) represent site S5: In a tetragonal

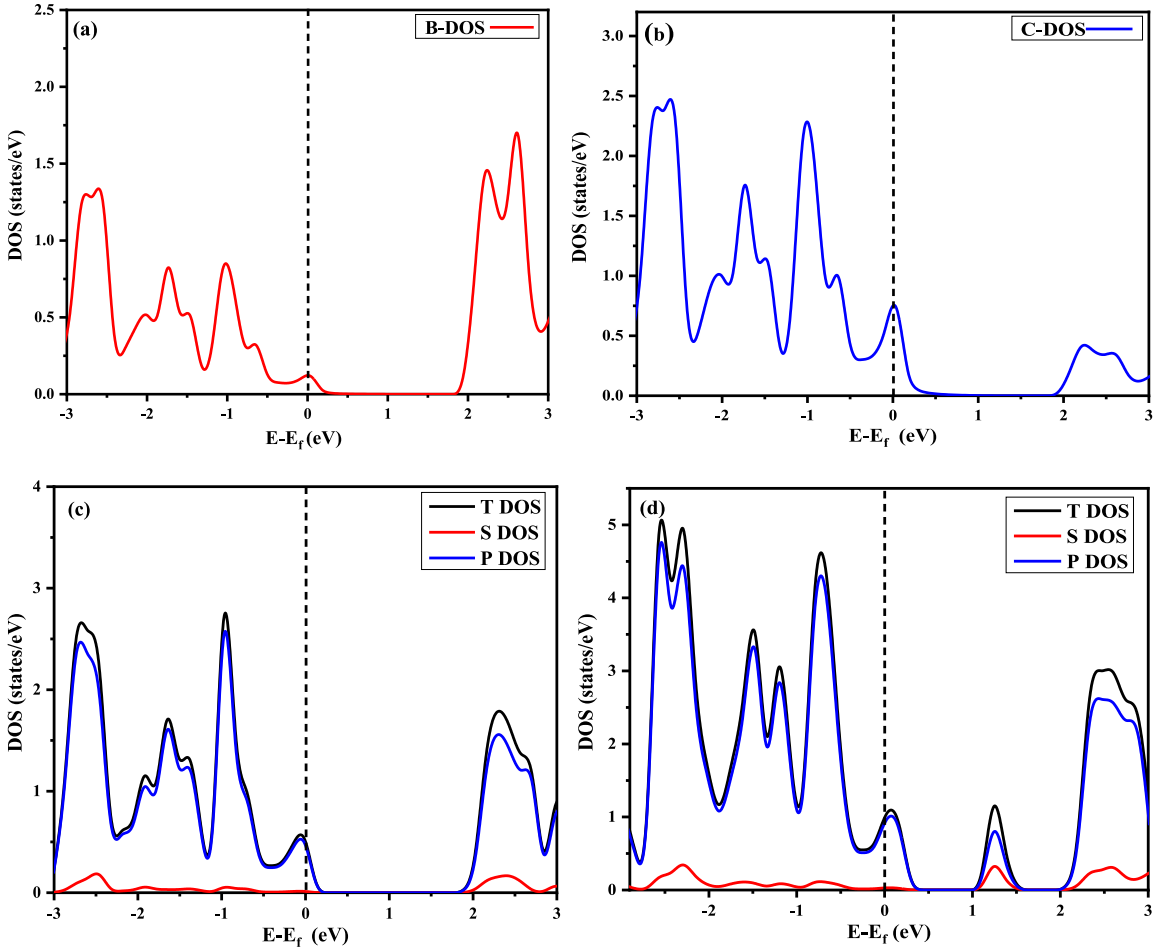

Fig. 2. (a) TDOS of B-atoms in B_4C_3, (b) TDOS of C-atoms in B_4C_3, (c) PDOS and TDOS of the B_4C_3 monolayer and (d) PDOS and TDOS of B_4C_3 with 1 Li intercalation.

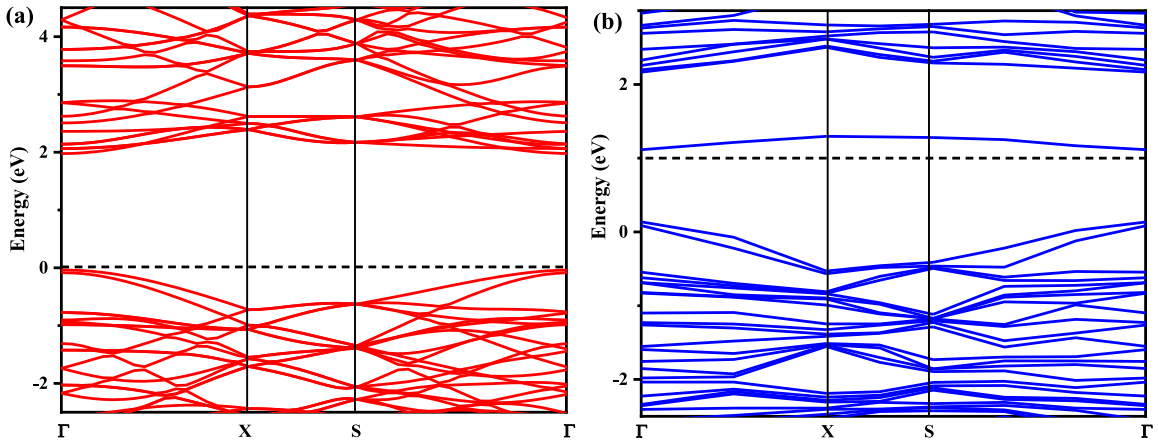

Fig. 3. Band structure of (a) pure B_4C_3 and (b) B_4C_3 with one Li atom.

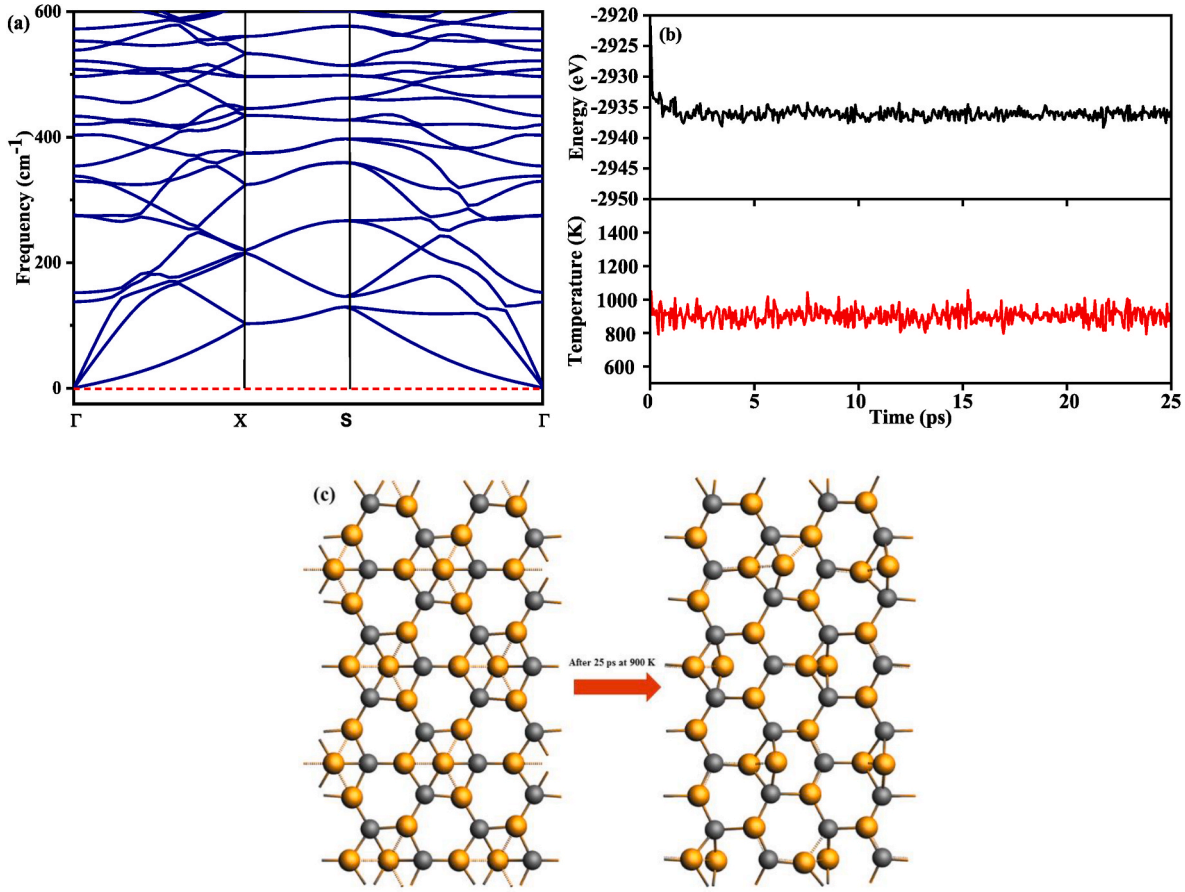

Fig. 4. (a) Phonon band structure of B_4C_3 monolayer, (b) AIMD calculation showing the change in energy and temperature over time and (c) snapshots of B_4C_3 monolayer before and after the simulation at 900 K.

shape between two C atoms and two B atoms and Fig. 5 (f) represent site S6: Between two B atoms and one C atom. The calculated value of lithiation energy at S1 using Equation (1) is 2.85 eV, resulting in an endothermic reaction, so this site is unfavorable. At the S2 site, the lithium atom is placed over a boron atom in the middle of the ring. The computed lithiation energy stands at −0.44 eV, representing the most favorable site as the reaction is exothermic. At the S3 site, the lithium atom is placed between C and B atoms, resulting in 0.7 eV lithiation energy, which is unsuitable (endothermic reaction). At the S4 site, lithium is placed over the carbon atom surrounded by four B-atoms. Lithiation energy is found to be 0.64 eV, which is unfavorable (endothermic reaction). At the S5 site, the lithiation energy is found to be 0.8 eV, which is also unfavorable. The lithiation energy for the S6 site is 0.85 eV. All sites with positive energy are not allowed.

3.5. Lithiation energy

B_4C_3 Structures with different lithium concentrations at different positions are given in Fig. 6. In Fig. 6 (a), a single lithium atom is positioned at the hexagon's centre above the boron atom, and the second

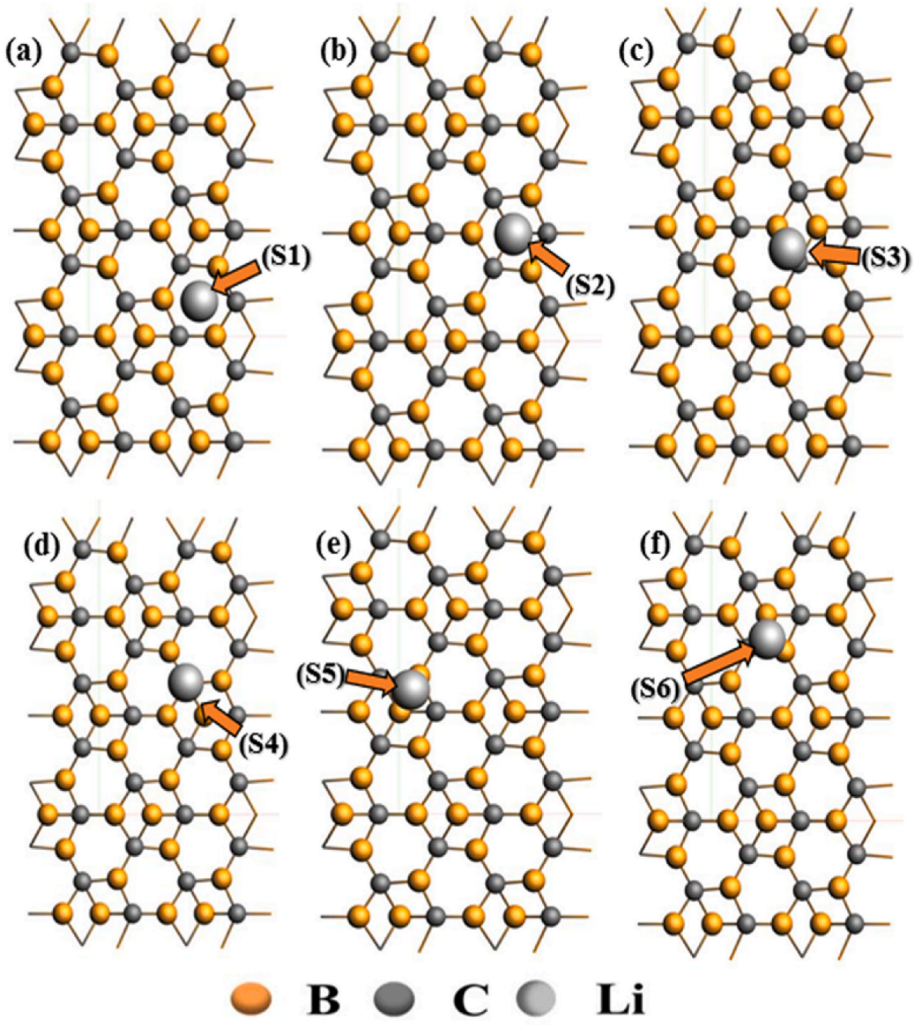

Fig. 5. Energy profiling by placing lithium atom in the host at (a) site S1 located in the centre of the hexagonal ring made by C and B atoms where the ring is vacant, (b) site S2 lies in the second type of ring over the B atom (c) site S3 situated between the B and C atom over their bond, (d) site S4 among four B atoms and over a C atom, (e) site S5 positioned in a tetragonal shape where two C atoms align with two B atoms and (f) site S6 which exists between two B atoms and 1 C atom.

Li is placed above the carbon atom along the z-axis. Fig. 6 (b) illustrates the adsorption of 5 Li atoms, three above the monolayer and two located beneath the host monolayer along the y-axis. Fig. 6 (c) depicts 7 Li atoms adsorbed on the surface; three are at the top of the 2D host layer and four are below the layer (along the x-axis). Fig. 6 (d) represents the host structure with 9 Li atoms adsorbed (view along the z-axis).

The calculations are carried out to determine the lithiation energy of B_4C_3 by using Equation (1) up to 29 lithium atoms, as shown in Fig. 9. The declining trend depicted in the graph indicates that the lithiation energy value decreases as more lithium atoms are introduced demonstrating the feasibility of the reaction, which turns out to be exothermic. According to that trend, lithiation energy will never give positive energy. When we get a positive energy value by using equation (1), it means that the host material will not adsorb further atoms over itself. But positive energy is not always necessary to finish our adsorption. Sometimes, we do not get positive energy, but by steric interaction calculations, Hirshfeld charge analysis and AIMD simulations, we learned that host material will not adsorb further atoms as saturation attains.

In the case of B_4C_3, the lithiation energy never becomes positive, so there is a need for a critical analysis of the lithiation process and the formation of dendrites. Fig. 7 (a) shows 29 lithium atoms adsorbed on the host material. We can visualize that no lithium atom leaves the surface of the host structure and doesn't push any lithium atom away from it. When the 30th Li is placed over the host structure, during the process of geometry optimization, it starts moving away from the surface as denoted by the arrowhead and starts making another layer of lithium atoms away from the surface, resulting in dendrite formation, as shown in Fig. 7 (b).

To explore the reason behind the lack of further absorption of Li atoms, steric interaction calculations are carried out. Fig. 7 (c) depicts that the 30th Li atom does not interact with the surface of the host material and does not take part in the charge transfer process.

Furthermore, instead of relying solely on calculating the lithiation energy based on equation (1), AIMD simulations were also carried out to check the feasibility of incorporating 29 Li atoms into the monolayer. Investigating the intercalation of lithium atoms without their aggregation into clusters is helpful. Fig. 8 (a) and 8 (b) show the stability of this configuration during AIMD simulations carried out at 400 K and 900 K respectively. The system's energy remains nearly constant, showing the host monolayer's stability. The snapshot of the host structure with intercalation of 30 lithium atoms after AIMD simulations for 25 ps at 400 K and 900 K are represented in Fig. 8 (c) and 8 (d) respectively. The close inspection of the structures exhibited the absence of breaking of bonds in the host structure and ruled out possible aggregation of Li atoms into clusters, which points to requisite structural stability and feasibility of the host monolayer as an anode in LIBs.

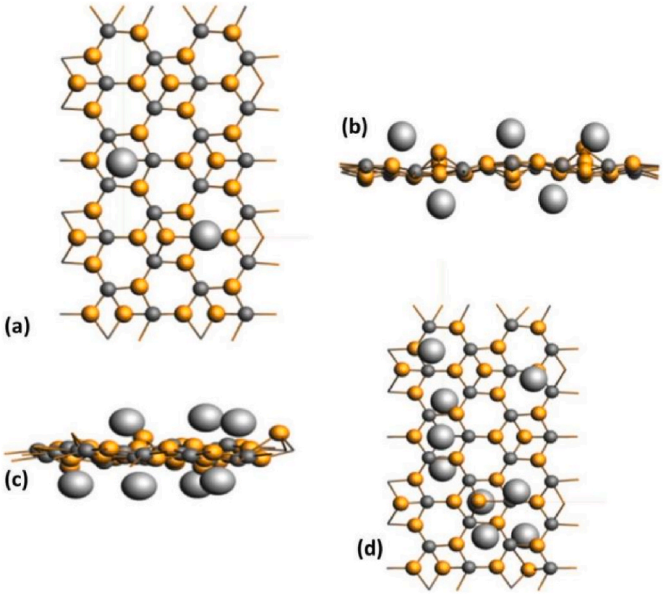

Fig. 6. Optimized B_4C_3 monolayer (a) z-axis view with 2 Li atoms, (b) y-axis view with 5 Li atoms, (c) x-axis view with 7 Li atoms and (d) z-axis view with 9 Li atoms intercalation.

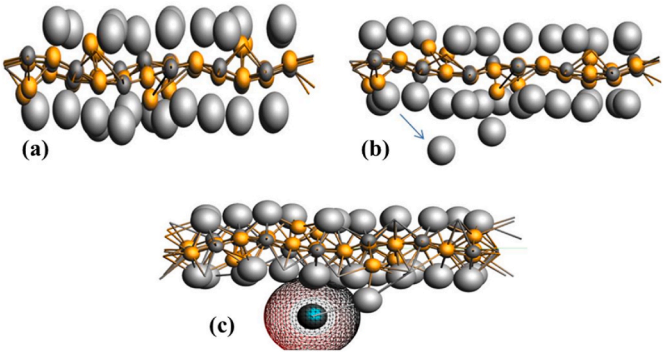

Fig. 7. (a) Snapshot of 29 Li atoms adsorbed on host B_4C_3, (b) Snapshot of 30th lithium atoms pushed away from the surface and (c) Steric interaction of separated lithium by the surface.

3.6. Storage capacity

The storage capacity of B_4C_3 is calculated by using equation (2) which comes 2770.21 $mAhg^{-1}$ and represented in Fig. 10. This is high value compared to commercially available anodes, as listed in Table 1. We used x as 29 in Equation (2) because the saturation of the host structure required 29 Li atoms intercalation, confirmed by steric interaction calculation depicted in Fig. 7 (c) and AIMD simulation explained in section 4.1 and Fig. 8.

3.7. Voltage profile

Voltage profiling is a crucial parameter to study the electrode performance in LIBs [60]. The maximum voltage value per Li for the host monolayer is 0.62 V/Li which is a reasonable value when compared to the previously reported anode materials depicted in Table 1 [28]. Fig. 11 illustrates the voltage profile of the B_4C_3 anode with a fluctuating behavior similar to the reported literature [61]. The voltage spikes occur due to minimal energy variance among the optimized energies of neighboring phases with similar characteristics. At a lithium concentration of 41%, the decline in potential becomes negligible, revealing a discernible plateau-shaped curve. The plateaus suggest the presence of a single-phase system within the battery during electrochemical processes. Some lithium/vacancy arrangements, which are not the lowest energy states, are marginally above the convex hull, making them potentially accessible. To incorporate temperature effects into computational voltage profiles, understanding the internal energy and entropy of the system after thermalization is necessary to minimize the temperature-dependent free energy. One common method for sampling the configuration space under specific conditions is the Metropolis Monte Carlo (MC) technique, which stochastically explores system states with their appropriate probabilities within a given statistical ensemble [62,63]. However, achieving convergence in thermodynamic ensemble averages with MC simulations typically demands millions of energy assessments and large atomic configurations, making them computationally challenging when using DFT.

3.8. Diffusion path

Climbing image nudge elastic band (CI-NEB) computations are utilized to find the migration pathways of lithium atoms within the host structure and only the three most feasible paths are reported along the x-axis, y-axis and diagonal. Cl-NEB is the improved method of NEB in which we get the highest energy image up to the critical point, optimizing energy across the band while reducing it in all other directions. Along each path, eight intermediate images are considered. Three cases are investigated: (a) is along the x-axis, (b) is along the y-axis and (c) is taken along the diagonals. The diffusion path along the x-axis and energy barrier is shown in Fig. 12 (a). The energy obstacle along the x-axis is 0.06 eV, making it highly conducive to intercalation. On the other hand, the diffusion path along the y-axis presents an energy barrier of 0.21 eV, marking it as the less advantageous option illustrated in Fig. 12 (b). The energy obstacles along the diagonal is 0.20 eV. This is the second most suitable path along the host, as shown in Fig. 12 (c).

3.9. Diffusion coefficient and ionic conductivity

This study involved computing the diffusion coefficient for Li diffusion over host B_4C_3 monolayer across a temperature range from 300 K to 900 K. These computations relied on Molecular Dynamics (MD) simulations employing the NVT ensemble and a Berendsen thermostat [64]. We derived the activation energy (E_a) and pre-exponential constant D_o values by plotting D versus 1/T using the Arrhenius Equation, as illustrated in Fig. 13 (a). The Mean Square Displacement (MSD) for the host monolayer was determined using Equation (6). The rate of ionic diffusion is important upon the interactions between diffusing ions and host atoms. The analysis of trajectories revealed faster diffusion at high temperatures attributed to rapid charging [65]. The ionic conductivity (σ) was computed utilizing Equation (8) and depicted in Fig. 13 (b). At room temperature 300 K, the host monolayer's diffusion coefficient and ionic conductivity were found to be 0.7×10^{-8} m^2/s and 0.78 S/m respectively. The diffusivity of Li atoms within the host monolayer that of reported anode materials for LIBs [50,66,67]. Amidst ongoing research endeavors aimed at identifying potential anode materials for LIBs [49,68,69], numerous novel anode materials have been developed [70–74]. However, further research efforts are imperative to comprehensively grasp the underlying mechanisms and devise new anode materials with enhanced electrochemical properties.

4. Conclusions

First-principles computations are utilized in the ADF modules Band and DFTB to explore the suitability of the B_4C_3 monolayer as a positive electrode in LIBs. Geometry optimization and absorption of Li on the B_4C_3 surface were performed, followed by determining optimal adsorption sites for Li atoms. The lithiation process was examined until the lithium atoms started dendrites formation and no charge was

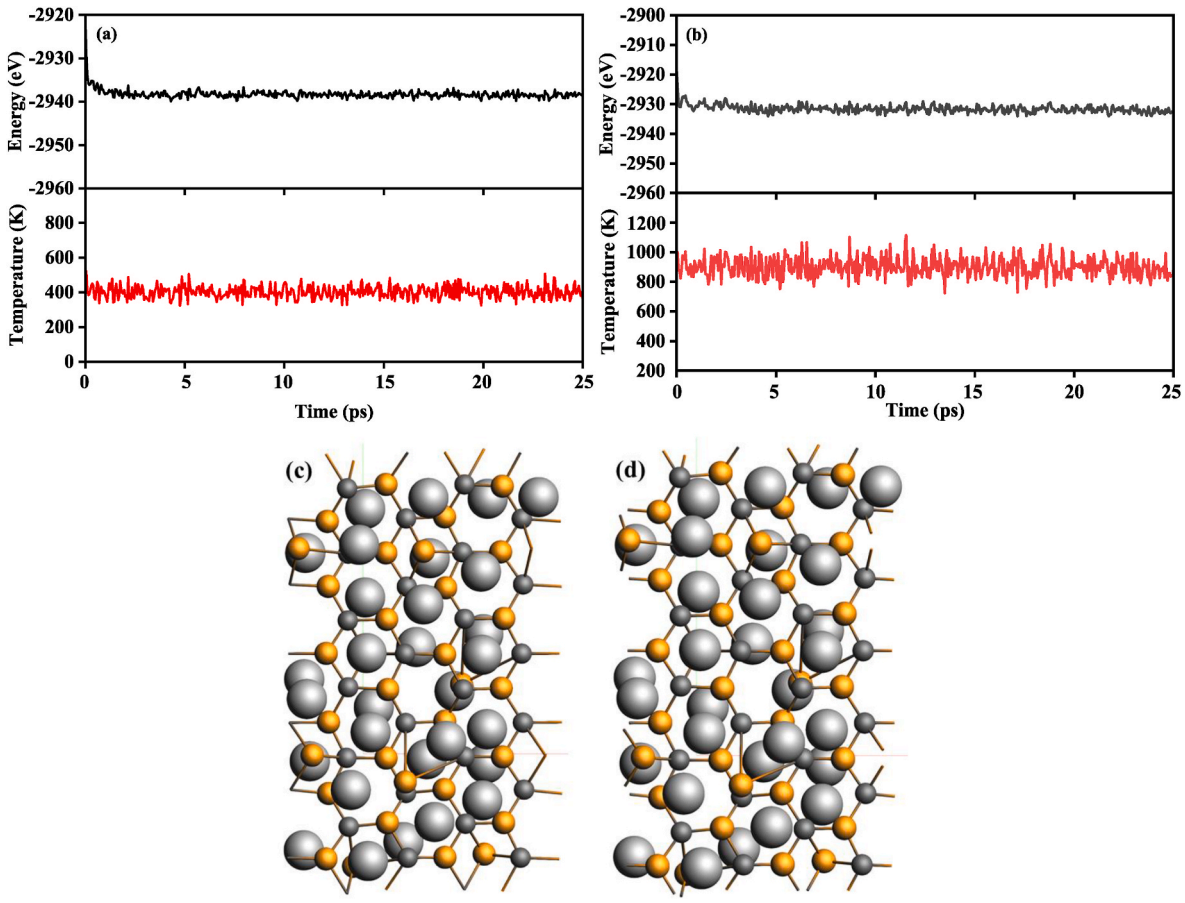

Fig. 8. (a) AIMD calculation showing the change in energy and temperature over time carried out (a) at 400 K, (b) at 900 K, (c) snapshots of 30 Li incorporation into B_4C_3 after simulations at 400 K and (d) snapshots of 30 Li incorporation into B_4C_3 after simulations at 900 K.

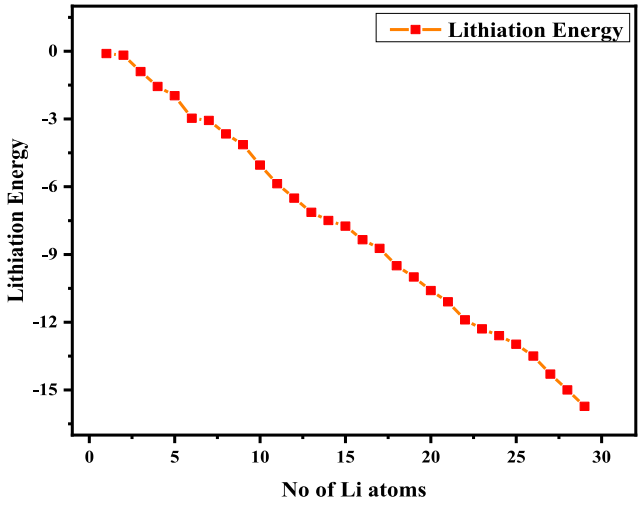

Fig. 9. The calculated variation in lithiation energy concerning lithium concentration in B_4C_3.

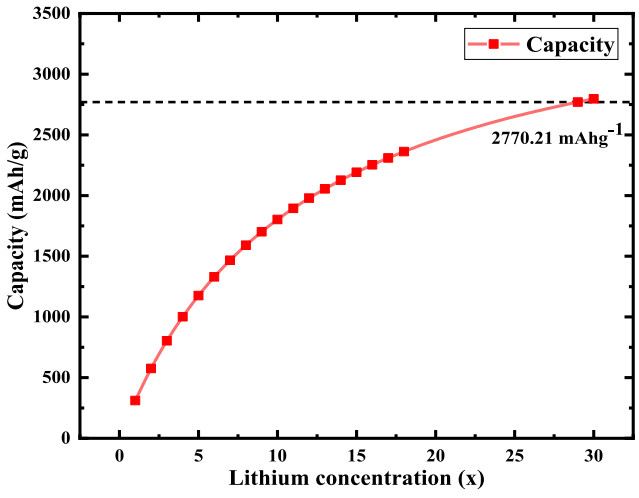

Fig. 10. Storage capacity as a function of lithium concentration.

transferred to the host, as confirmed by steric interaction studies and AIMD simulations. The computed capacity of B_4C_3 is 2770.2 mAh/g. The diffusion path energy barrier of Li was studied using the Cl-NEB method, with the minimum value of the energy barrier along the x-axis being 0.06 eV. The determined open circuit voltage is 0.62 V per Li atom, with a diffusion coefficient and ionic conductivity of 0.7×10^{-8} m^2/s and 0.78 S/m respectively, at 300K. The findings offer insightful perspectives into the behaviour and performance of B_4C_3 as a promising anode material in LIBs. The calculated storage potential emphasizes its elevated energy capacity, positioning it as a favorable candidate for upcoming battery applications. The analysis of lithiation energy and diffusion characteristics sheds light on the electrochemical behaviour of B_4C_3, helping to understand the mechanisms and kinetics involved in the lithiation process.

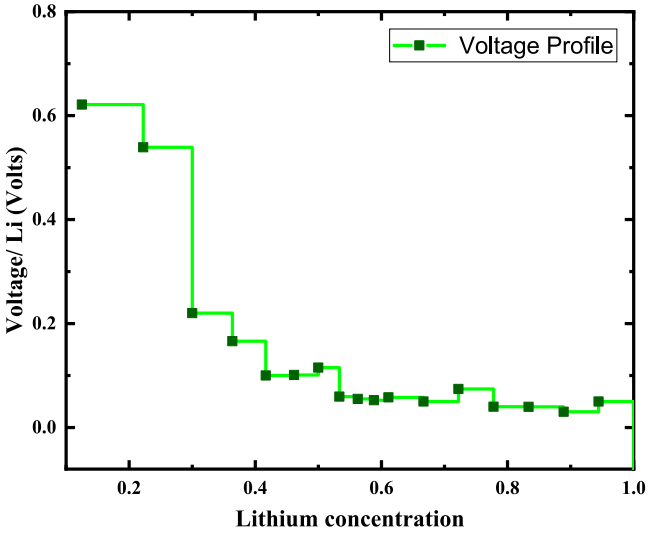

Fig. 11. The voltage profile calculated for the B_4C_3 Monolayer.

Ethical Approval

Not applicable.

Funding

The ADU author acknowledges financial support from Abu Dhabi University's Office of Research and Sponsored Programs. Grant number: [19300638,19300791].

CRediT authorship contribution statement

Abdul Majid: Supervision, Software, Project administration, Investigation, Conceptualization. **Usama Najam:** Writing – original draft, Formal analysis, Data curation. **Sheraz Ahmad:** Writing – review & editing, Validation, Methodology. **Mohammad Alkhedher:** Writing – review & editing, Visualization, Validation.

Declaration of Competing Interest

The authors declare that they have no known competing financial interests or personal relationships that could have appeared to influence the work reported in this paper

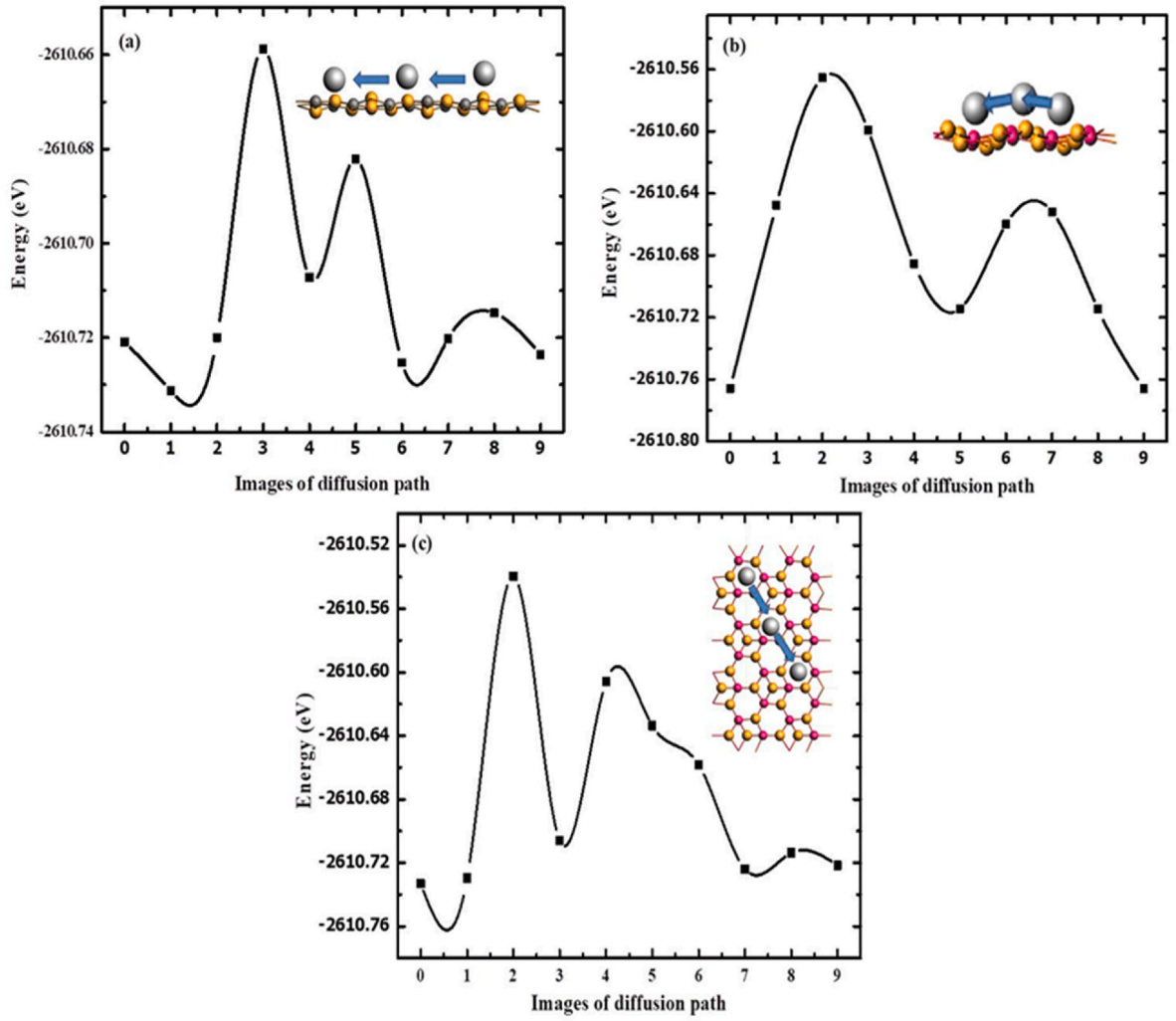

Fig. 12. Diffusion path along **(a)** the x-axis of the host monolayer with the transition barrier of 0.06 eV, **(b)** the y-axis with a transition barrier of 0.21 eV and (c) the diagonal path with a transition energy barrier of 0.20 eV.

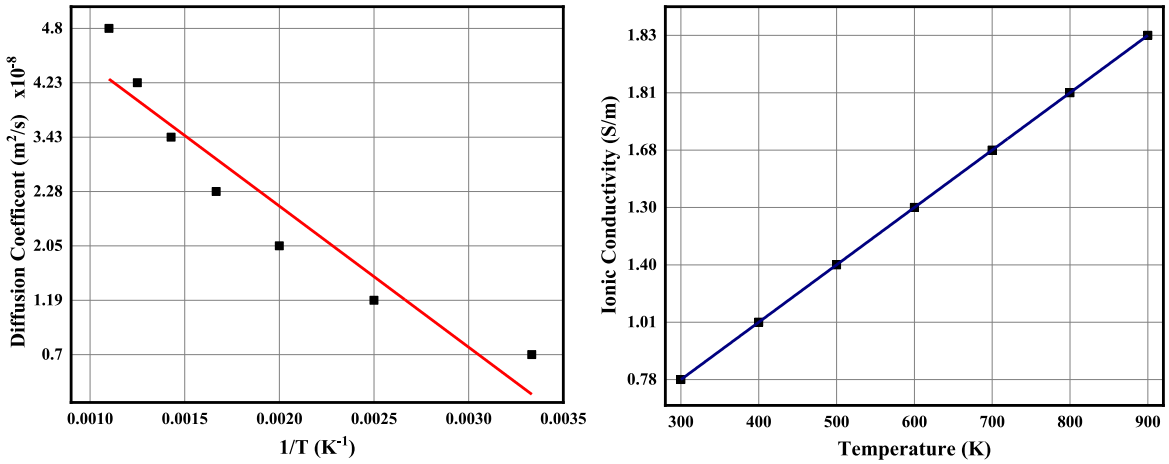

Fig. 13. **(a)** Diffusion coefficient as a function of 1/T, where T in is Kelvin and (b) Ionic conductivity as a function of temperature.

Data availability

Data will be made available on request.

References

[1] S. Ahmed, et al., First principles study of layered CrGeTe3 as lithium intercalation compound, J. Electrochem. Soc. 169 (4) (2022) 040557.
[2] A.K. Mohanty, et al., Sustainable composites for lightweight and flame retardant parts for electric vehicles to boost climate benefits: a perspective, Composites Part C: Open Access 12 (2023) 100380.
[3] J. Twidell, Renewable Energy Resources, Routledge, 2021.
[4] Y. Liang, et al., A review of rechargeable batteries for portable electronic devices, InfoMat 1 (1) (2019) 6–32.
[5] Z. Zhu, et al., Rechargeable batteries for grid scale energy storage, Chem. Rev. 122 (22) (2022) 16610–16751.
[6] A. Fatima, et al., First principles study of layered silicon carbide as anode in lithium ion battery, Int. J. Quant. Chem. 122 (11) (2022) e26895.
[7] T.R. Jow, et al., Factors limiting Li+ charge transfer kinetics in Li-ion batteries, J. Electrochem. Soc. 165 (2) (2018) A361.
[8] L. Zhao, et al., Revisiting the roles of natural graphite in ongoing lithium-ion batteries, Adv. Mater. 34 (18) (2022) 2106704.
[9] H.B. Son, et al., All-impurities scavenging, safe separators with functional metal-organic-frameworks for high-energy-density Li-ion battery, Adv. Funct. Mater. (2023) 2302563.
[10] Y. Yang, et al., 2D layered materials for fast-charging lithium-ion battery anodes, Small (2023) 2301574.
[11] G. Li, et al., Recent advances and perspectives of microsized alloying-type porous anode materials in high-performance Li-and Na-ion batteries, Energy Mater 2 (2022) 200020.
[12] L. Shi, T. Zhao, Recent advances in inorganic 2D materials and their applications in lithium and sodium batteries, J. Mater. Chem. A 5 (8) (2017) 3735–3758.
[13] B. Liu, et al., Amorphous modulation of atomic Nb-O/N clusters with asymmetric coordination in carbon shells for advanced sodium-ion hybrid capacitors, Small (2023) 2308263.
[14] D. Chen, et al., Two-dimensional square metal organic framework as promising cathode material for lithium-sulfur battery with high theoretical energy density, J. Colloid Interface Sci. 613 (2022) 435–446.
[15] A. Kabiraj, S. Mahapatra, High-throughput assessment of two-dimensional electrode materials for energy storage devices, Cell Reports Physical Science 3 (1) (2022).
[16] L. Sun, et al., Recent progress and future perspective on practical silicon anode-based lithium ion batteries, Energy Storage Mater. 46 (2022) 482–502.
[17] X. Zhou, et al., Facile synthesis and electrochemical properties of two dimensional layered MoS2/graphene composite for reversible lithium storage, J. Power Sources 251 (2014) 264–268.
[18] Y. Zhu, et al., Graphene and graphene oxide: synthesis, properties, and applications, Adv. Mater. 22 (35) (2010) 3906–3924.
[19] Z. Xu, et al., A promising anode material for sodium-ion battery with high capacity and high diffusion ability: graphyne and graphdiyne, RSC Adv. 6 (30) (2016) 25594–25600.
[20] W. Li, et al., Ultrafast and directional diffusion of lithium in phosphorene for high-performance lithium-ion battery, Nano Lett. 15 (3) (2015) 1691–1697.
[21] S. Najmaei, et al., Synthesis and defect investigation of two-dimensional molybdenum disulfide atomic layers, Accounts Chem. Res. 48 (1) (2015) 31–40.
[22] C. Xu, et al., Large-area high-quality 2D ultrathin Mo2C superconducting crystals, Nat. Mater. 14 (11) (2015) 1135–1141.
[23] T. Xu, et al., Moisture-enabled electricity from hygroscopic materials: a new type of clean energy, Adv. Mater. (2023) 2209661.
[24] J.-m. Xie, et al., Advances in sulfur-doped carbon materials for use as anodes in sodium-ion batteries, N. Carbon Mater. 38 (2) (2023) 305–316.
[25] C. Li, et al., Two dimensional borophene nanomaterials: recent developments for novel renewable energy storage applications, Prog. Solid State Chem. (2023) 100416.
[26] K. Aswathi, N. Baskaran, First-principles study of beryllium substituted borophene as an anode material for Li/Na-ion batteries, Computational Condensed Matter 37 (2023) e00845.
[27] H. Li, et al., Scalable production of few-layer boron sheets by liquid-phase exfoliation and their superior supercapacitive performance, ACS Nano 12 (2) (2018) 1262–1272.
[28] X. Luo, et al., Predicting two-dimensional boron–carbon compounds by the global optimization method, J. Am. Chem. Soc. 133 (40) (2011) 16285–16290.
[29] J.B. Matsoso, et al., Co-doping graphene with B and N heteroatoms for application in energy conversion and storage devices, ChemNanoMat 8 (7) (2022) e202200134.
[30] P. Novák, D. Goers, M.E. Spahr, Carbon materials in lithium-ion batteries, Carbons for Electrochemical Energy Storage Systems (2010) 263–328.
[31] A. Rosenkranz, et al., 2D nano-materials beyond graphene: from synthesis to tribological studies, Appl. Nanosci. 10 (2020) 3353–3388.
[32] A. Majid, et al., Modeling of inert gas sensors using first principles methods, IEEE Sensor. J. 23 (2023) 18118–18124.
[33] S. Noreen, et al., Emerging 2D-Nanostructured materials for electrochemical and sensing Application-A review, Int. J. Hydrogen Energy 47 (2) (2022) 1371–1389.
[34] M. Wan, et al., Two-dimensional BeB2 and MgB2 as high capacity Dirac anodes for Li-ion batteries: a DFT study, J. Phys. Chem. C 126 (23) (2022) 9642–9651.
[35] X. Yu, et al., Metallic B2C monolayer as a promising anode material for Li/Na ion storage, Chem. Eng. J. 406 (2021) 126812.
[36] A. Mahmood, et al., in: Photocatalytic properties of novel two-dimensional B4C3/g-C3N4 van der Waals heterojunction with moderate bandgap and high carrier mobility: A theoretical study vol. 278, 2020 119310.
[37] A.E. Senturk, A.S. Oktem, A.E.S. Konukman, Thermal conductivity and mechanical properties of graphene-like BC2, BC3 and B4C3 46 (12) (2020) 879–888.
[38] J. Shen, et al., First-Principles Observation of Bonded 2D B4C3 Bilayers 6 (20) (2021) 13218–13224.
[39] N.E. Ofili, Adsorption of Actinides on Mineral Surfaces, The University of Manchester, 2021 (United Kingdom).
[40] K. Huang, Y. Liu, H. Liu, First-principles study of the adsorption and diffusion mechanisms of lithium dendrite growth, Mol. Simulat. (2022) 1–8.
[41] K. Hayamizu, Direct relations between ion diffusion constants and ionic conductivity for lithium electrolyte solutions, Electrochim. Acta 254 (2017) 101–111.
[42] L.J. Miara, et al., Li-ion conductivity in Li 9 S 3 N, J. Mater. Chem. A 3 (40) (2015) 20338–20344.
[43] S. Ahmed, et al., Ab-initio characterization of B4C3 monolayer as a toxic gases sensing material, Appl. Surf. Sci. 544 (2021) 148877.
[44] M.I. khan, S. Khalid, A. Majid, S.S. Alarfaji, Empowering spintronics performance of 3d transition metal adsorbed B4C3 monolayer: a DFT outlook, J. Phys. Chem. Solid. 187 (2024) 111599.
[45] U. Nosheen, et al., First-principles insight into a B4C3 monolayer as a promising biosensor for exhaled breath analysis, J. Electron. Mater. 51 (11) (2022) 6568–6578.
[46] H. Chang, et al., B4C3 monolayer with impressive electronic, optical, and mechanical properties: a potential metal-free photocatalyst for CO2 reduction under visible light, J. Phys. Chem. C 123 (41) (2019) 25091–25101.
[47] H. Benzidi, et al., Arsenene monolayer as an outstanding anode material for (Li/Na/Mg)-ion batteries: density functional theory, Phys. Chem. Chem. Phys. 21 (36) (2019) 19951–19962.
[48] Y. Jing, et al., Metallic VS2 monolayer: a promising 2D anode material for lithium ion batteries, J. Phys. Chem. C 117 (48) (2013) 25409–25413.

[49] X. Lv, et al., Metallic FeSe monolayer as an anode material for Li and non-Li ion batteries: a DFT study, Phys. Chem. Chem. Phys. 22 (16) (2020) 8902–8912.
[50] J. Park, S.A. Fatima, A DFT study of TiC3 as anode material for Li-ion batteries, Appl. Surf. Sci. 638 (2023) 158024.
[51] G. Yuan, et al., Monolayer Zr2B2: a promising two-dimensional anode material for Li-ion batteries, Appl. Surf. Sci. 480 (2019) 448–453.
[52] N. Shekh, D. Chodvadiya, P.K. Jha, Rational design of h-AlC monolayer as anode material for Mg-ion battery: a DFT study, Energy Storage 5 (3) (2023) e415.
[53] C. Zhu, et al., Ultrahigh capacity 2D anode materials for lithium/sodium-ion batteries: an entirely planar B 7 P 2 monolayer with suitable pore size and distribution, J. Mater. Chem. A 8 (20) (2020) 10301–10309.
[54] N. Duhan, B. Chakraborty, T.D. Kumar, 2-dimensional biphenylene monolayer as anode in Li ion secondary battery with high storage capacity: acumen from density functional theory, Appl. Surf. Sci. 629 (2023) 157171.
[55] Y. Guo, et al., YS2 monolayer as a high-efficient anode material for rechargeable Li-ion and Na-ion batteries, Solid State Ionics 345 (2020) 115187.
[56] Y. Wu, et al., Highly stable TiOF monolayer as anode material for the applications of Li/Na-ion batteries, Appl. Surf. Sci. 574 (2022) 151296.
[57] Y. Wu, H. Li, J. Hou, A first-principle study of FeB6 monolayer as a potential anode material for Li-ion and Na-ion batteries, Comput. Mater. Sci. 190 (2021) 110273.
[58] K. Rajput, et al., Ca2C MXene monolayer as a superior anode for metal-ion batteries, 2D Mater. 8 (3) (2021) 035015.
[59] Y.-Y. Wu, et al., Two-dimensional tetragonal Ti2BN: a novel potential anode material for Li-ion batteries, Appl. Surf. Sci. 513 (2020) 145821.
[60] T.P. Senftle, A.C. Van Duin, M.J. Janik, Methane activation at the Pd/CeO2 interface, ACS Catal. 7 (1) (2017) 327–332.
[61] V. Sharma, K. Ghatak, D. Datta, Amorphous germanium as a promising anode material for sodium ion batteries: a first principle study, J. Mater. Sci. 53 (20) (2018) 14423–14434.
[62] N. Metropolis, et al., Equation of state calculations by fast computing machines, J. Chem. Phys. 21 (6) (1953) 1087–1092.
[63] K. Binder, D.W. Heermann, K. Binder, Monte Carlo Simulation in Statistical Physics, vol. 8, Springer, 1992.
[64] M.V. Koudriachova, N.M. Harrison, S.W. de Leeuw, Diffusion of Li-ions in rutile. An ab initio study, Solid State Ionics 157 (1–4) (2003) 35–38.
[65] R. Trivedi, D. Bandyopadhyay, Study of adsorption and dissociation pathway of H2 molecule on MgnRh (n= 1–10) clusters: a first principle investigation, Int. J. Hydrogen Energy 41 (44) (2016) 20113–20121.
[66] X. Zhao, et al., Screening MXenes for novel anode material of lithium-ion batteries with high capacity and stability: a DFT calculation, Appl. Surf. Sci. 569 (2021) 151050.
[67] X. Ji, Y. Wang, J. Zhang, Understanding the anisotropic strain effects on lithium diffusion in graphite anodes: a first-principles study, Phys. B Condens. Matter 539 (2018) 66–71.
[68] Z. Xu, et al., DFT investigation of capacious, ultrafast and highly conductive hexagonal Cr 2 C and V 2 C monolayers as anode materials for high-performance lithium-ion batteries, Phys. Chem. Chem. Phys. 19 (11) (2017) 7807–7819.
[69] J. Zhang, et al., Blue-AsP monolayer as a promising anode material for lithium-and sodium-ion batteries: a DFT study, Phys. Chem. Chem. Phys. 23 (9) (2021) 5143–5151.
[70] Y. Xing, et al., A first principle study of 2D single-layer SiP as anode material for lithium-ion battery and sodium-ion battery, Phys. Chem. Chem. Phys. 26 (2024) 7072–7082.
[71] X. Xiong, et al., Tetragonal BN monolayer: a high-performance anode material for lithium-ion batteries, Comput. Mater. Sci. 232 (2024) 112626.
[72] S. Ma, et al., Two dimensional AlB4 as high-performance anode material for Li/Na-ion batteries, Appl. Surf. Sci. 648 (2024) 159024.
[73] S.S. Rifah, et al., Exploring the anodic performance of ScSeS and TiSeS monolayers of modified transition metal dichalcogenides for Mg ion batteries via DFT calculations, Phys. Chem. Chem. Phys. 26 (2024) 6667–6677..
[74] M. Wang, et al., TiNX (X= F, Cl) monolayer as potential anode materials for Li/Na-ion batteries applications, J. Energy Storage 78 (2024) 110105.